Promoted crystallisation and cationic ordering in thermoelectric Cu 26 V 2 Sn 6 S 32 colusite by eccentric vibratory ball milling

Michal Hegedüs, Marcela Achimovičová, Hongjue Hui, Gabin Guelou, P. Lemoine, Ismail Fourati, Jean Juraszek, B. Malaman, Peter Baláž, Emmanuel Guilmeau

Promoted crystallisation and cationic ordering in thermoelectric $Cu_{26}V_2Sn_6S_{32}$ colusite by eccentric vibratory ball milling

Michal Hegedüs,[1] Marcela Achimovičová,[2] Hongjue Hui,[3] Gabin Guélou,[3] Pierric Lemoine,[4] Ismail Fourati,[5] Jean Juraszek,[5] B. Malaman,[6] Peter Baláž,[2] Emmanuel Guilmeau[3,*]

[1] Synthon, s.r.o., Brněnská 32, 678 01 Blansko, Czech Republic

[2] Institute of Geotechnics, Slovak Academy of Sciences, Watsonova 45, 04001 Košice, Slovakia

[3] CRISMAT, CNRS, Normandie Univ, ENSICAEN, UNICAEN, 14000 Caen, France

[4] Univ Rennes, CNRS, ISCR - UMR 6226, F-35000 Rennes, France

[5] Normandie Univ, INSA Rouen, UNIROUEN, CNRS, GPM, 76000 Rouen, France

[6] Institut Jean Lamour, UMR 7198 CNRS – Université de Lorraine, 2 allée André Guinier-Campus ARTEM, BP 50840, 54011 Nancy Cedex, France

Corresponding author: emmanuel.guilmeau@ensicaen.fr

Abstract

A pristine colusite $Cu_{26}V_2Sn_6S_{32}$ was successfully synthesised on a 100 g scale via mechanochemical reaction in an industrial eccentric vibratory ball mill followed by spark plasma sintering (SPS) at 873 K. The milling of elemental precursors from 1 up to 12 hours was performed and the prepared samples were investigated in details by X-ray powder diffraction, Mössbauer spectroscopy, scanning electron microscopy, and thermoelectric property measurements. The results point to the formation of a high purity and high crystallinity non-exsoluted colusite phase after SPS process ($P\bar{4}3n$, a = 10.7614(1) Å) in the case of a 12 h

milled sample. In comparison, samples milled for 1-6 h displayed small quantities of binary Cu-S phases and vanadium core-shell inclusions, leading to a V-poor/Sn-rich colusite with higher degree of structural disorder. These samples exhibit lower electrical conductivity and Seebeck coefficient while an increase in the total thermal conductivity is observed. This phenomenon is explained by a higher reactivity and grain size reduction upon prolonged milling and by a weak evolution of the chemical composition from a partly disordered V-poor/Sn-rich colusite phase to a well-ordered stoichiometric $Cu_{26}V_2Sn_6S_{32}$ colusite, which leads to a decrease in carrier concentration. For all samples, the calculated *PF* values, around 0.7-0.8 mW m^{-1} K^{-2} at 700 K, are comparable to the values previously achieved for mechanochemically synthesised $Cu_{26}V_2Sn_6S_{32}$ in laboratory mills. This approach thus serves as an example of scaling-up possibility for sulphur-based TE materials and supports their future large-scale deployment.

Introduction

Waste heat harvesting through conversion into electricity by thermoelectric (TE) materials is essential for future energy management.[1–3] The advent of new low-toxicity and cost-effective inorganic TE materials offers opportunities to recover waste heat more efficiently and economically using highly reliable systems that neither possess any moving parts nor produce any noise or vibration. Generally, best thermoelectric performances are obtained in metal tellurides, which are expensive and toxic.[1,4] To conciliate efficiency with environmental and cost constraints, it is required to replace tellurium (Te) with a less-toxic and more earth-abundant homologous element. Compared with Te, sulphur (S) has a lighter mass, smaller atomic radius, and larger electronegativity. The lighter mass should lead to higher phonon frequencies/Debye temperature and hence higher lattice thermal conductivity (κ_L). Thus, sulphides are naively thought to have a slightly higher thermal conductivity, and a lower power factor, $PF = S^2\rho^{-1}$, and hence a lower figure of merit, $ZT = S^2T\rho^{-1}\kappa^{-1}$, where S is the

Seebeck coefficient, ρ the electrical conductivity, κ the thermal conductivity, and T is the absolute temperature. As a consequence, TE sulphides have been somewhat overlooked with respect to tellurides and selenides despite their more significant diversity of crystal structures and compositions.

Thus, research focusing on TE sulphides has recently regained momentum.[5] Cu-based ternary and quaternary sulphides with complex structures were especially identified as potential TE materials for mid-temperature range applications.[6] They can exhibit very low thermal conductivity combined with a semiconducting or degenerate semiconducting (metallic-like) behaviour, allowing to reach relatively high *ZT* values. A non-exhaustive list includes: tetrahedrites $Cu_{12}Sb_4S_{13}$,[7–13], colusites $Cu_{26}T_2M_6S_{32}$ (T = V, Nb, Ta, Cr, Mo, W; M = Sn, Ge),[14–20] germanite derivatives $Cu_{22}Fe_8Ge_4S_{32}$,[21] stannoidite $Cu_8Fe_3Sn_2S_{12}$,[22] bornite Cu_5FeS_4,[23–26] chalcopyrite $CuFeS_2$,[27] isocubanite $CuFe_2S_3$,[28] mohite Cu_2SnS_3,[29] kesterite Cu_2ZnSnS_4,[30,31] and $Cu_4Sn_7S_{16}$.[32]

Among those materials, colusites with the general formula $Cu_{26}T_2M_6S_{32}$ (T = V, Nb, Ta, Cr, Mo, W; M = Sn, Ge) can exhibit high *PF* values close to 2 mW m^{-1} K^{-2},[20,33] and *ZT* values close to 1 at 700 K[19,20,34] (See references given in Table 1). Colusites have a complex cubic structure (space group $P\bar{4}3n$, $a \approx$ 10.6-10.8 Å) with 66 atoms per unit cell, which can be described as a sphalerite-type network of corner-sharing CuS_4 and MS_4 tetrahedra (**Figure 1**). These tetrahedra are ordered in such way that the "sphalerite" unit cell is doubled in all 3 directions and the T cation occupies the *2a* interstitial position at the corners and centre of this $2a_{Sph}\times 2a_{Sph}\times 2a_{Sph}$ supercell.

The thermoelectric performance can be controlled to a large extent thanks to cationic substitution on different crystallographic sites or by altering the stoichiometry, as shown in **Table 1**. It was especially shown that the reduced lattice thermal conductivity (κ_L) in colusites was attributed to several kinds of phonon scatterers, *i.e.* Cu/Sn antisite defects, interstitial

defects, antisite defects, and split Cu site,[34–37] mainly induced by the processing conditions used. Based on these observations, it is essential to point out that the processing step plays a key role in determining the final thermoelectric properties,[34,36] especially in the case of structurally complex sulphides. Reproducibility and scalability of their synthesis represent another challenge that is yet to be addressed by current research in this field. The mechanochemistry seems to be the most effective, low-cost, and eco-friendly approach towards scalable synthesis of Cu-based sulphides.[38,39] This has been recently demonstrated on ternary and quaternary copper sulphides, such as tetrahedrite $Cu_{12}Sb_4S_{13}$,[40–44] $Cu_4Sn_7S_{16}$,[32] bornite Cu_5FeS_4,[24,25] colusite $Cu_{26}V_2Sn_6S_{32}$,[16,20,34,36,45,46] germanite derivative $Cu_{22}Fe_8Ge_4S_{32}$,[21,47,48] stannoidite $Cu_8Fe_3Sn_2S_{12}$,[22] isocubanite $CuFe_2S_3$,[28] mohite Cu_2SnS_3,[49,50] stannite Cu_2FeSnS_4,[51] kesterite Cu_2ZnSnS_4,[52–56] and mawsonite $Cu_6Fe_2SnS_8$,[57] that can be readily prepared by ball milling in a planetary mill by direct reaction of elements or binary sulphides. The possibility to prepare pristine colusite by mechanochemical synthesis was first reported by Bourgès *et al.*[16], but only for small batches of 5g. With the aim to synthesise large quantity of colusite in one step and with high reproducibility, we investigated the scalability of pristine colusite $Cu_{26}V_2Sn_6S_{32}$ synthesis using an industrial eccentric vibratory ball mill. The present study reports on the effect of milling time on the sample purity, crystallinity and thermoelectric performances of pristine colusite $Cu_{26}V_2Sn_6S_{32}$.

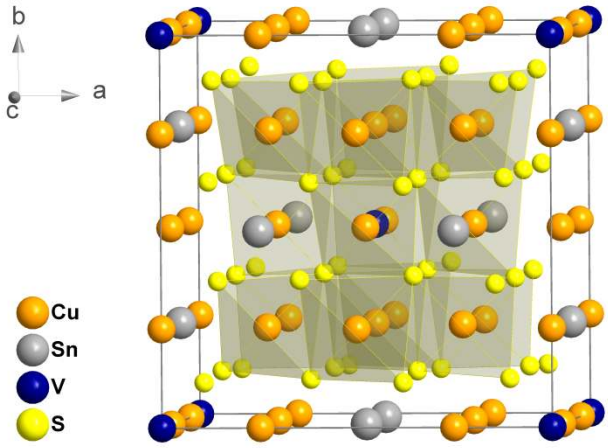

Figure 1. Representation of the crystal structure of pristine colusite $Cu_{26}V_2Sn_6S_{32}$.

Table 1. Review on the influence of the preparation method and chemical composition on the thermoelectric performances (represented by *ZT* values) of colusites. HP: Hot-Pressing; MA: Mechanical Alloying; SPS: Spark Plasma Sintering.

Preparation method	Nominal composition	*ZT*	Reference
melt + HP	$Cu_{26}V_2M_6S_{32}$ (M = Ge, Sn)	0.55/0.73 @663 K	Suekuni *et al.*[14]
melt + HP	$Cu_{26-x}Zn_xV_2Sn_6S_{32}$ (x=0-3)	0.20-0.55 @660 K	Kim *et al.*[15]
melt + HP	$Cu_{26-y}V_2Sn_{6-z}S_{32}$ (y=0-2; z =0-1)	0.30-0.62 @660 K	Kim *et al.*[15]
MA + SPS	$Cu_{26-x}Zn_xV_2Sn_6S_{32}$ (x = 0-2)	0.3-0.4 @700 K	Bourgès *et al.*[16]
melt + HP	$Cu_{26}T_2Sn_6S_{32}$ (T = Nb, Ta)	0.6-0.8 @670 K	Kikuchi *et al.*[17]
melt + SPS	$Cu_{24}M'_2V_2Ge_6S_{32}$ (M' = Ni, Co)	0.42/0.5 @690 K	Bouyrie *et al.*[18]
melt + HP	$Cu_{26}T_2M_{6-x}S_{32}$ (T = Nb, Ta; M = Sn, Ge, x=0, 0.5)	0.6-1.0 @670 K	Bouyrie *et al.*[19]
melt + HP	$Cu_{24}Nb_2V_2Ge_6M'_xS_{32}$ (M' = Co, Ni, Fe; x < 1)	0.55-0.7 @665 K	Bouyrie *et al.*[58]
MA + SPS	$Cu_{26}V_2Sn_6S_{32}$	0.93 @675 K	Bourgès *et al.*[34]
MA + SPS	$Cu_{26}T_2Ge_6S_{32}$ (T = Cr, Mo, W)	0.65-0.86 @700 K	Pavan Kumar *et al.*[20]
MA + SPS	$Cu_{26}V_2Sn_6S_{32}$	0.70 @673 K	Guélou *et al.*[36]

Experimental Section

Mechanochemical solid state syntheses were performed in an industrial eccentric vibratory ball mill ESM 656-0.5 ks (Siebtechnik, Germany) working under the following conditions: 5 L steel satellite milling chamber attached to the main corpus of the mill, tungsten carbide balls with a diameter of 35 mm and total mass of 25 kg, 80% ball filling, amplitude of the mill 20 mm, rotational speed of the eccenter 960 min^{-1}, argon atmosphere, total feed of reaction precursors 100 grams per batch. The milling was performed from 1h to12 hours. Elemental powders of copper (99% Merck, Germany), vanadium (Alfa Aesar 99.5%), tin (99%

Nihon Seiko, Japan), and sulphur (99% CG-Chemikalien, Germany) were used as starting reactants. The amounts of each element were calculated based on the $Cu_{26}V_2Sn_6S_{32}$ stoichiometry.

After completion of the milling programs, the resulting pulverised powder was shaped and densified using SPS (FCT HPD 25) at 873 K for 30 minutes (heating and cooling rate of 100 K/min) under a pressure of 64 MPa using graphite dies of 10 mm diameter and a slight overpressure of 30 hPa (Ar), in order to prevent both oxidation and sulphur volatilisation. The final thickness of the pellets was around 8 mm with a geometrical density in excess of 90 % of the crystallographic value.

X-ray powder diffraction (XRPD) patterns of the milled samples were acquired at room temperature using a Bruker D8 Advance Vario 1 two-circle diffractometer in θ-2θ Bragg-Brentano geometry equipped with a Cu X-ray tube, a Ge (111) monochromator (*i.e.* λ = 1.54056 Å) and a Lynx Eye detector. The XRPD data were analysed by Rietveld refinement using the FullProf and WinPlotr software packages.[59,60]

^{119}Sn Mössbauer spectrometry was performed on polycrystalline powders at room temperature in transmission geometry and constant-acceleration mode. The source was ^{119m}Sn source in $CaSnO_3$ matrix with an activity of ~130 MBq. For the velocity calibration, a ^{57}Fe Mössbauer spectrum of a α-Fe foil at RT was collected using a ^{57}Co source mounted at the other side of the spectrometer transducer. Isomer shifts (δ) are given with respect to SnO_2 at room temperature. Least-squares fits of the experimental data were performed using the histogram method assuming Lorentzian lines.

Observations of fractured cross-sections of densified pellets by scanning electron microscopy (SEM) were performed using a ZEISS Supra 55 field emission scanning electron microscope.

The electrical resistivity (ρ) and Seebeck coefficient (S) were measured simultaneously on ingots, from 300 K up to 700 K using an ULVAC-ZEM3 device under partial helium pressure. A NETZSCH LFA-457 apparatus was used for measuring the thermal diffusivity under argon flow. The thermal conductivity (κ) was determined as the product of the geometrical density, the thermal diffusivity, and the theoretical heat capacity calculated by the Dulong−Petit approximation. The Wiedemann−Franz law, using a Lorenz number estimated from the relationship $L = 1.5 + \exp(-|S|/116)$,[61] was used to calculate the lattice thermal conductivity by subtracting the electronic contribution to the total thermal conductivity ($\kappa_L = \kappa - \kappa_e$). The estimated measurement uncertainties are 6% for the Seebeck coefficient, 8% for the electrical resistivity, 11% for the thermal conductivity, and 16% for the final figure of merit, ZT.[62]

Results and discussion

The XRPD patterns of the elemental powders milled for a period of time ranging from 1 h to 12 h are shown in **Figure 2**. First, it should be noted that, after only one hour of milling, no diffraction peaks arising from elemental precursors (Cu, V, Sn, S) are observed. This is closely connected to highly negative Gibbs formation energies of binary and ternary sulphides, especially in Cu-S based systems.[63] Rapid formation of $Cu_{2-x}S$ and Cu_2SnS_3 has been recently reported.[49,50] These nanocrystalline sulphides are formed within the very first minutes of milling in an explosive way. Secondly, the relatively low crystallinity of the powders leads to high full width at half maximum (FWHM) values of diffraction peaks. Consequently, it is not possible to observe the low angle diffraction peaks characteristic of the colusite structure and therefore to confirm formation of the colusite phase during the ball-milling process only. Indeed, the main diffraction peaks observed on these XRPD data can be attributed to a (Cu,V,Sn)S sphalerite-derivative phase such as poorly crystalline colusite $Cu_{26}V_2Sn_6S_{32}$, or mohite

Cu_2SnS_3, phases. Finally, diffraction peaks corresponding to a covellite CuS phase are observed on the XRPD patterns, especially for short milling times. In previous studies,[49,50] it was shown that, during ball-mill processes, binary and ternary phases are formed first, followed by more complex sulphides in later stages of milling, annealing or sintering. Hence, the most likely admixture in samples after ball-milling is covellite CuS with either mohite Cu_2SnS_3 or a cubic (Cu,V,Sn)S sphalerite-derivative. However, due to the significant overlap of Bragg reflections of these phases with colusite, the formation of the latter cannot be excluded, especially at longer milling times. Importantly, traces of vanadium metal and Cu_3VS_4 sulvanite are detected in the powder samples (arrows) with shorter milling times (1h, 3h, 6h), but are absent in the sample milled during 12h. As discussed below in SEM section, this has a huge impact over the purity of the sintered products, as well as chemical composition and final crystallinity of colusite phase.

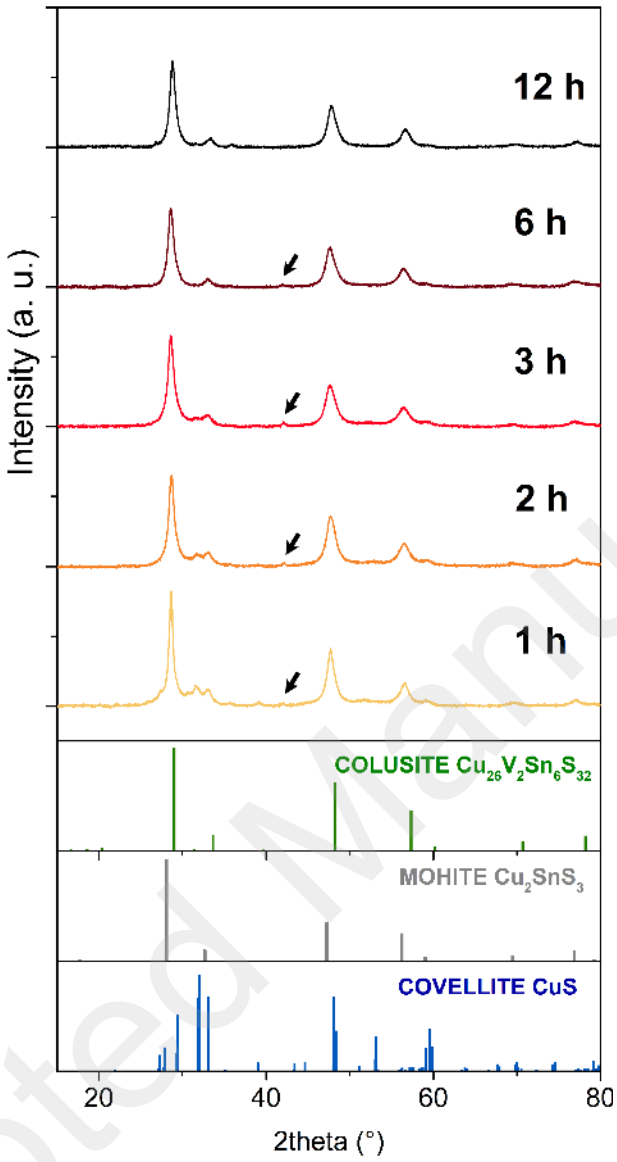

Figure 2. XRPD patterns of ball-milled elemental mixtures at milling times ranging from 1 h up to 12 h.

The XRPD patterns of four selected samples after SPS processing (milled for 1, 3, 6, and 12 hours) were closely examined (**Figure 3** and **S1**). Contrary to the XRPD patterns recorded on ball-milled samples, the diffraction peaks at low angles, characteristic of the colusite $Cu_{26}V_2Sn_6S_{32}$ crystal structure ($P\bar{4}3n$, a ≈ 10.77 Å, Cu on 6*d*, 8*e*, and 12*f* sites, V on 2*a* site, Sn on 6*c* site, and S on 8*e* and 24*i* sites), confirm the formation of this complex copper-based

sulphide even after 1 hour of milling followed by SPS treatment (**Figure 3a**). When the mixture is subjected to longer milling periods, the shape of the diffraction peaks related to colusite structure evolves. Indeed, the integral intensity of the superstructure 211, 321, and 332 reflections evolves from 1 to 6 hours of milling and seems stable for higher milling times. This can be explained by a slight evolution of the chemical composition of the colusite phase coupled with an increased (micro)structural ordering with increasing milling time (see SEM section). This is supported by a decrease in the unit cell parameter of the colusite phase with increasing milling duration,[33–35,37] respectively from 10.7819(1) Å to 10.7614(1) Å for 1h+SPS and 12h+SPS samples. All structural data and reliability factors are provided in **Table 2** and **Table S1-S4.** These results confirm the important role played by both milling times and SPS process on phase crystallisation. Finally, these patterns also evidence extra diffraction peaks of weak intensity indicating the presence of secondary phases, corresponding to digenite $Cu_{2-x}S$ ($Fm\bar{3}m$, a ≈ 5.56 Å) and covellite CuS ($P6_3/mmc$, a ≈ 3.79 Å, c ≈ 16.36 Å) phases in 1h+SPS (≈ 5 wt.% and 1 wt.%, respectively, **Figure 3a**) and 3h+SPS samples (≈ 2 wt.% and 3 wt.%, respectively, **Figure S1a**), and covellite in 6h+SPS sample (≈ 1 wt.%, **Figure S1b**). It should be mentioned that XRPD data analysis indicates the contamination of the 6h+SPS sample by SiO_2 quartz of aragonite structure (≈ 1 wt.%) typically used for cleaning of the milling equipment, and of the 12h+SPS sample by traces of WC phase (< 1 wt.%) arising from abrasion of the milling medium (**Figure 3b**). Nevertheless, these results indicate that 12 hours of milling allow to produce large quantity (100 grams) of powder, which, after spark plasma sintering at 873 K, leads to a high purity pristine colusite material (**Figure 3b**).

Table 2. Structural data and reliability factors from Rietveld refinements of the ball-milled colusite $Cu_{26}V_2Sn_6S_{32}$ samples after SPS process.

Sample	1h + SPS	3h + SPS	6h + SPS	12h + SPS
a (Å)	10.7819(1)	10.7634(1)	10.7634(1)	10.7614(1)
V (Å^3)	1253.39(2)	1252.44(2)	1246.95(1)	1246.25(2)
R_{Bragg}	5.51	6.57	3.85	2.59
R_F	5.14	8.03	5.35	4.32
R_{wp}	11.30	15.60	10.30	9.47
R_{exp}	8.03	10.57	8.04	7.32
χ^2	1.97	2.18	1.65	1.67

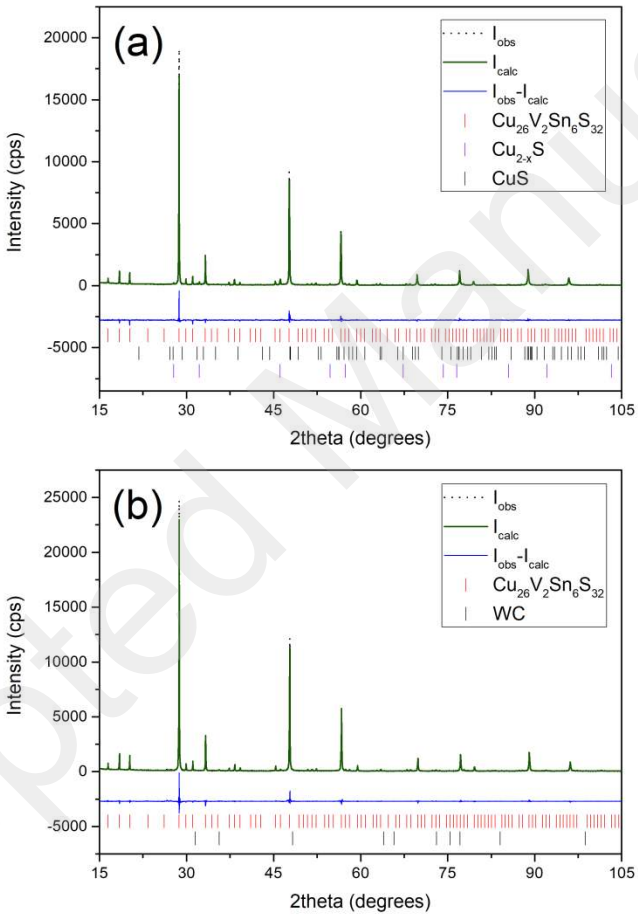

Figure 3. Rietveld refinements of XRPD patterns of (a) 1h+SPS and (b) 12h+SPS samples.

In order to better understand the influence of milling times on the structural disorder/crystallinity of colusite, ^{119}Sn Mössbauer spectroscopy measurements were performed at room temperature. This technique allows to obtain important information on the local environment of tin atoms in solids (electronic structure and chemical bonding),[64] and consequently, indicates indirectly the degree of structural order-disorder in Sn-colusite.[35] ^{119}Sn Mössbauer spectra of selected sintered samples are shown in **Figure 4**. The spectrum of the 1h+SPS sample (**Figure 4a**) exhibits a single peak centred near 1.5 mm s^{-1}, with a shape distinct from a pure Lorentzian line. For the best fit of the experimental data, we use a combination of a singlet and a quadrupolar doublet (green and red curves in **Figure 4a**, respectively), as for the fitting procedure described by Candolfi *et al*.[35] Both components have the same refined isomer shift value (δ = 1.45 mm s^{-1}) which is characteristic of +IV oxidation state of Sn atoms, and almost the same relative spectral area (49% and 51%, respectively). These two contributions indicate the presence of Sn atoms on more than one crystallographic site in the crystal structure, one of them being slightly distorted, as evidenced by the refined value of the quadrupole splitting of the doublet (ΔE_Q = 1.02 ± 0.07 mm s^{-1}). The same fitting procedure has been applied for the Mössbauer spectrum of the 6h+SPS sample (**Figure 4b**), exhibiting a line with narrower shape. The refined value of the quadrupole splitting of the doublet is reduced (ΔE_Q = 0.83 ± 0.18 mm s^{-1}) and the relative spectral area of the single line is increased (66 %), in agreement with a progressive ordering of the colusite phase with milling time as evidenced by XRPD analyses. This is further corroborated by the results obtained for the 12h+SPS sample for which the Mössbauer spectrum (**Figure 4c**) can be fitted with only a singlet with refined isomer shift and linewidth values of δ = 1.48 ± 0.01 mm s^{-1} and Γ = 1.10 ± 0.07 mm s^{-1}, respectively. This indicates that almost all the Sn atoms are located on a high symmetry site such as the 6*c* crystallographic site,[35] and confirms the high quality of the produced colusite material at the highest milling time. Note that, in the case of 1h+SPS and 12h+SPS samples, a doublet (~2%

of total spectral area, blue curve in **Figures 4a and 4c**) has been added to reproduce the slight shoulder of the peak near the zero-velocity position. This doublet is attributed to traces of SnO_2 impurity with a volume fraction too small to be detectable by XRPD.

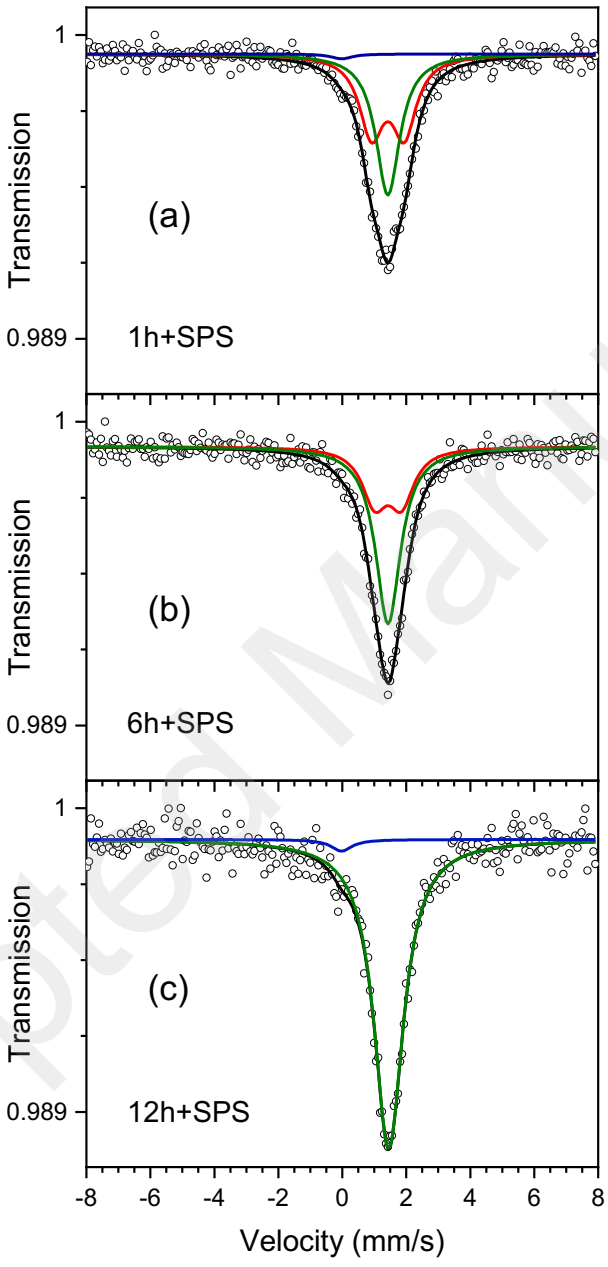

Figure 4. ^{119}Sn Mössbauer spectra at 295 K of (a) 1h+SPS, (b) 6h+SPS and (c) 12h+SPS samples.

The microstructures of ball-milled elemental mixtures and fractured cross-section of densified pellets are given in **Figure S2** and **5**, respectively. All powders exhibit similar particle

morphology and size distribution after ball-milling, as shown in the typical microstructure displayed in **Figure S2**. Prior to SPS treatment, the powders consist of large agglomerates made of particles of different sizes. The similarity between each batch of powder is in good agreement with the XRPD data and the rapid formation of nanocrystalline sulphides in less than 1 h of ball-milling. After SPS, the grain morphology appears isotropic, as expected from the cubic crystal structure of colusite, and the grain size ranges between 1 and 5 μm (**Figure 5**). It can be observed that the grain size tends to decrease with increasing milling time, which is self-evident in **Figure 5d** for 12h+SPS sample. Such feature is consistent with the more complete crystallisation in 12h+SPS sample due to the higher reactivity of the powders, as discussed in the structural analysis section above. Then, the formation of larger grains is favoured by reactive sintering in powders subjected to a ball-milling period shorter than 6h.

Back-scattered electron microscopy (BSE) coupled with EDS analysis confirms the complete crystallisation and homogeneity of the colusite phase for the 12h+SPS sample (**Figure 6, right**). The BSE-EDS analysis clearly shows the presence of vanadium-rich core-shell structures in 1h+SPS (**Figure S3, left**), 3h+SPS (**Figure S3, right**) and 6h+SPS (**Figure 6, left**) samples, consistent with our previous work,[36] and confirming the established formation mechanism. The latter has been demonstrated to be a rapid reaction between the Cu, Sn and S, forming a vanadium-poor colusite matrix that progressively accommodates the remaining vanadium metal. A core-shell structure of vanadium/sulvanite/V-rich/Sn-poor colusite is formed, surrounded by a V-poor/Sn-rich colusite matrix (**Figure S4**). It must be noted that the size of the vanadium particles tends to decrease from 1h+SPS to 3h-6h+SPS samples, and disappear in the 12h+SPS sample, in agreement with the XRD patterns presented in **Figure 2**. For short milling times (≤ 6h), the powders are insufficiently pre-reacted during ball-milling and the SPS step does not complete the crystallisation of the colusite phase, leaving artefacts of the formation mechanism in the form of vanadium-rich core-shell structures and off-stoichiometric

colusite matrix. This is also consistent with the cationic elemental analysis from EDS (**Table S5**), in which the vanadium content within the matrix progressively increases from a V-poor/Sn-rich colusite to the expected Cu:V:Sn ratio of 26:2:6. Note that the presence of vanadium metal and surrounding layers of Cu_3VS_4 sulvanite in SPS samples was missed by the XRD analysis because of the scarcity of vanadium and the close structural relationship between colusite and sulvanite, the main reflections of the latter overlapping those of the former. Colusite is also known to stabilise despite significant deviations from the ideal stoichiometry 26:2:6:32.[65] The crystallisation of Sn-rich colusites for short milling times (≤ 6h) is also in good agreement with the Mössbauer data (**Figure 4**), which indicate the presence of Sn atoms on more than one crystallographic site in the crystal structure and the evolution of the unit cell parameter of colusite determined by XRPD refinements (**Table 2**). This highlights the importance of milling time investigations for the fabrication of chalcogenides to favour complete crystallisation during the subsequent synthesis/sintering step.

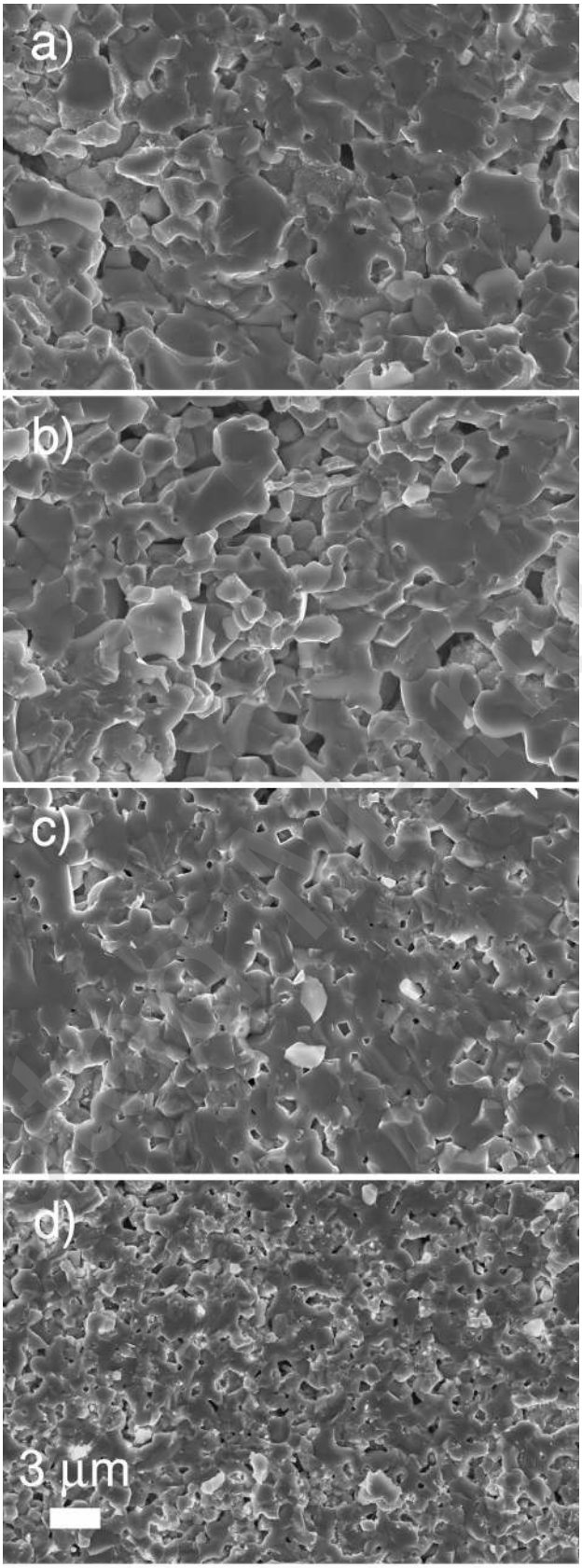

Figure 5. Micrographs of the fractured cross-sections of the sintered pellets for different ball-milling times (a) 1h, (b) 3h, (c) 6h and (d) 12h.

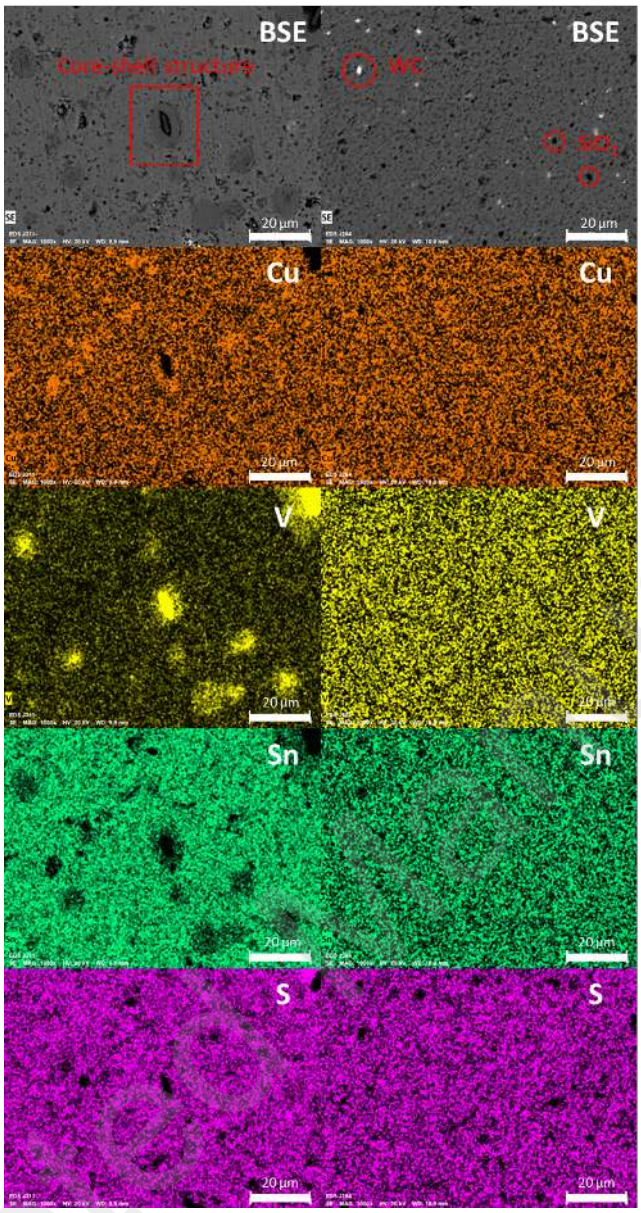

Figure 6. BSE micrographs and corresponding EDS elemental analysis maps for the samples 6h + SPS (left column) and 12h + SPS (right column).

The temperature dependences of the electrical resistivity and Seebeck coefficient are displayed in **Figure 7**. All exhibit a *p*-type degenerate-semiconducting behaviour in agreement with first-principle electronic structure calculations and experimental data.[14,34] The magnitudes of both the electrical resistivity and Seebeck coefficient are similar for the 1h+SPS, 3h+SPS and

6h+SPS samples, and range around 30 μV K^{-1} and 0.4 mΩ cm at RT, respectively. Those values are in good agreement with the results obtained for small batches (5g) of colusite $Cu_{26}V_2Sn_6S_{32}$ mechanochemically synthesised in a laboratory mill (Fritsch Pulverisette 7 Premium Line) of elemental precursors, and densified by SPS using similar conditions (873 K/45 min/64 MPa).[16,34] These electrical properties confirm the relatively good purity and crystallinity of the samples even for a ball-milling time as short as 1h, in agreement with the XRPD and SEM analyses. In the 12h+SPS sample, the electrical resistivity and Seebeck coefficient slightly increase over the whole temperature range, consistent with a slight decrease in the carrier concentration. This trend is probably linked to a higher purity and reactivity of the 12h ball-milled powder leading to a complete crystallisation of a more stoichiometric colusite phase during SPS and the absence of the vanadium core-shell structures observed by SEM for short milling times (≤ 6h). This hypothesis is strongly supported by the smaller grain size in this sample (after SPS), as shown in **Figure 5d**, and the BSE-EDS analyses presented in **Figure S3-6 and Table S5**. As expected, the heightened reactivity of the 12h ball-milled powder further leads to a better crystallinity, as confirmed by Rietveld refinements of XRPD data and ^{119}Sn Mössbauer spectroscopy in the previous sections. Note that the measured charge carrier concentration, considering the experimental error, does not vary significantly between the samples, remaining between 8.5×10^{21} and 9×10^{21} cm^{-3}, due to the slight variation of Seebeck coefficient between 1h, 3h, 6h, and 12h+SPS samples. Overall, the changes in Seebeck coefficient and in the electrical resistivity with milling time compensate each other and *PF* values, around 0.7-0.8 mWm^{-1} K^{-2} at 700 K (**Fig. 7e**), are retained for all samples. These values are comparable to those achieved in small batches of $Cu_{26}V_2Sn_6S_{32}$ colusites.[16,34] Heating and cooling measurements (displayed in **Figure S5**) of the electrical resistivity and Seebeck coefficient in ZEM3 revealed that the measurements in 1h and 3h+SPS samples are not reversible, due to the presence of a large quantity of secondary phases and "less reacted"

colusite powders. In contrary, the reversibility is enhanced in 6h and 12h+SPS samples. Further in-depth investigations are needed to address the long-term chemical stability of the as-prepared materials using industrial eccentric vibratory ball-milling. Especially, the chemical sensitivity of colusite against impurities from grinding media (WC, silica) must be studied in details.

The temperature dependence of the thermal conductivity for all samples is presented in **Fig. 7c**. All evidence the same temperature dependence characterised by a decrease in the thermal conductivity from 300 K to 700 K. For 1h+SPS, 3h+SPS and 6h+SPS samples, the thermal conductivities are comparable over the whole temperature range, in agreement with the electrical transport properties. The thermal conductivity drops down significantly in 12h+SPS sample as a result of a significantly reduced electronic contribution. Indeed, the lattice thermal conductivities (**Fig. 7d**) are found rather comparable regardless of the milling time. This suggests that the decrease in grain size, down to 1 µm in 12h+SPS sample, as well as the vanadium core-shell inclusions, are not sufficient to enhance phonon scattering through an increased density of grain boundaries. The values of the total and lattice thermal conductivities are also in good agreement with the results obtained in small batches of $Cu_{26}V_2Sn_6S_{32}$ colusites.[16,34] Finally, the figure-of-merit *ZT* ranges between 0.3 and 0.35 at 700 K among the investigated samples, which is comparable with values reported for undoped colusites synthesised by laboratory mechanochemical synthesis and densified at relatively low temperature (873 K).[16,34,36] The sintering of such colusite powders at high temperature is now required to promote structural disorder[34–36] and to achieve lower lattice thermal conductivity and higher *ZT* values in large ingots.

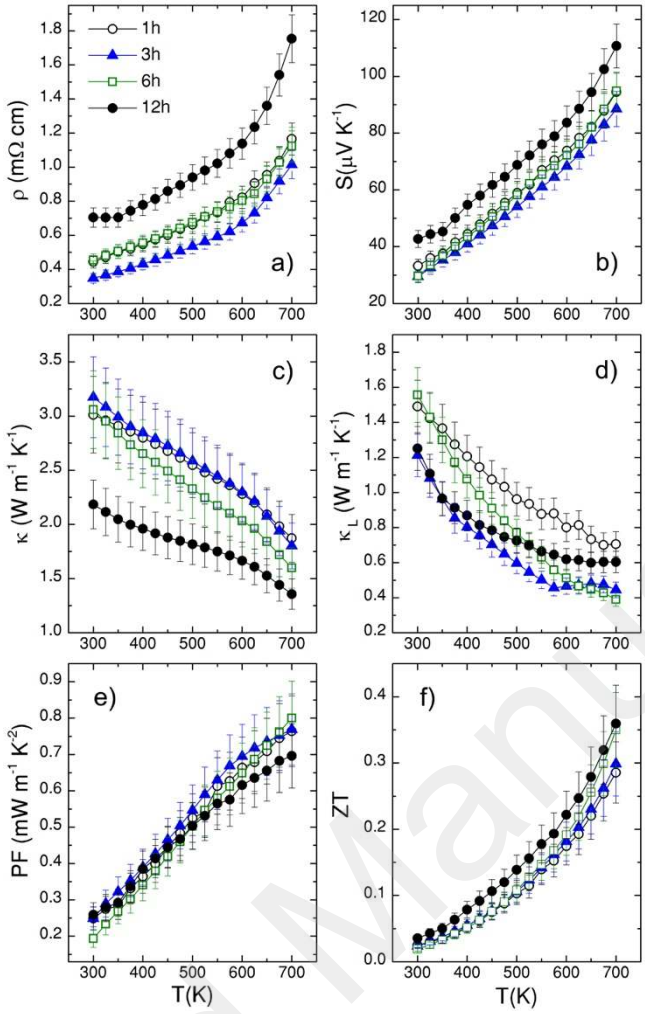

Figure 7. Temperature dependence of the (a) electrical resistivity (ρ), (b) Seebeck coefficient (S), (c) thermal conductivity (κ), (d) lattice thermal conductivity (κ_L), (e) power factor (PF), and (f) figure of merit ZT of $Cu_{26}V_2Sn_6S_{32}$ with different ball-milling times.

Conclusions

The pristine colusite $Cu_{26}V_2Sn_6S_{32}$ was successfully synthesised by mechanical alloying of elemental precursors in an eccentric industrial vibratory ball mill under argon atmosphere at 100 grams scale. Ball-milled powders showed quintessential polydisperse character with mostly submicronic particles. The need for prolonged milling before SPS treatment, in order to achieve higher crystallinity and purity materials, is emphasised. This is closely related to the enhanced

reactivity of milled powders during SPS treatment. The obtained *ZT* value of bulk colusites using powders synthesised in an industrial mill is comparable to the values obtained in laboratory mills. Overall, the applied approach can serve as a scalable route for the mass production of ternary and quaternary sulphides for a wide range of applications.

Acknowledgments

The authors (M.A., P.B.) acknowledge support of the Slovak Research and Development Agency (project APVV-0357-18). E.G. and G.G. would like to thank Christelle Bilot and Jérôme Lecourt for technical support and acknowledge the financial support of Institut Carnot ESP (project MASTER), FEDER and Normandy Region.

References

1 D. M. Rowe, *Thermoelectrics Handbook: Macro to Nano*, CRC Press, Boca Raton, FL, ed. D. M., 2006.

2 X. Shi, J. Zou and Z. Chen, *Chem. Rev.*, 2020, **120**, 7399.

3 R. Freer and A. V. Powell, *J. Mater. Chem. C*, 2020, **8**, 441–463.

4 J. R. Sootsman, D. Y. Chung and M. G. Kanatzidis, *Angew. Chemie - Int. Ed.*, 2009, **48**, 8616–8639.

5 S. Hébert, D. Berthebaud, R. Daou, Y. Bréard, D. Pelloquin, E. Guilmeau, F. Gascoin, O. Lebedev and A. Maignan, *J. Phys. Condens. Matter*, 2016, **28**, 013001.

6 A. V. Powell, *J. Appl. Phys.*, 2019, **126**, 100901.

7 X. Lu, D. T. Morelli, Y. Xia, F. Zhou, V. Ozolins, H. Chi, X. Zhou and C. Uher, *Adv.*

Energy Mater., 2013, **3**, 342–348.

8 K. Suekuni, K. Tsuruta, T. Ariga and M. Koyano, *Appl. Phys. Express*, 2012, **5**, 051201.

9 K. Suekuni, K. Tsuruta, M. Kunii, H. Nishiate, E. Nishibori, S. Maki, M. Ohta, A. Yamamoto and M. Koyano, *J. Appl. Phys.*, 2013, **113**, 043712.

10 Y. Bouyrie, C. Candolfi, V. Ohorodniichuk, B. Malaman, A. Dauscher, J. Tobola and B. Lenoir, *J. Mater. Chem. C*, 2015, **3**, 10476–10487.

11 R. Chetty, A. Bali and R. C. Mallik, *J. Mater. Chem. C*, 2015, **3**, 12364–12378.

12 T. Barbier, P. Lemoine, S. Gascoin, O. I. Lebedev, A. Kaltzoglou, P. Vaqueiro, A. V. Powell, R. I. Smith and E. Guilmeau, *J. Alloys Compd.*, 2015, **634**, 253–262.

13 P. Vaqueiro, G. Guélou, A. Kaltzoglou, R. I. Smith, T. Barbier, E. Guilmeau and A. V. Powell, *Chem. Mater.*, 2017, **29**, 4080–4090.

14 K. Suekuni, F. S. Kim, H. Nishiate, M. Ohta, H. I. Tanaka and T. Takabatake, *Appl. Phys. Lett.*, 2014, **105**, 132107.

15 F. S. Kim, K. Suekuni, H. Nishiate, M. Ohta, H. I. Tanaka and T. Takabatake, *J. Appl. Phys.*, 2016, **119**, 175105.

16 C. Bourgès, M. Gilmas, P. Lemoine, N. Mordvinova, O. I. Lebedev, E. Hug, V. Nassif, B. Malaman, R. Daou and E. Guilmeau, *J. Mater. Chem. C*, 2016, **4**, 7455–7463.

17 Y. Kikuchi, Y. Bouyrie, M. Ohta, K. Suekuni, M. Aihara and T. Takabatake, *J. Mater. Chem. A*, 2016, **4**, 15207–15214.

18 Y. Bouyrie, V. Ohorodniichuk, S. Sassi, P. Masschelein, A. Dauscher, C. Candolfi and B. Lenoir, *J. Electron. Mater.*, 2017, **46**, 2684–2690.

19 Y. Bouyrie, M. Ohta, K. Suekuni, Y. Kikuchi, P. Jood, A. Yamamoto and T. Takabatake, *J. Mater. Chem. C*, 2017, **5**, 4174–4184.

20 V. Pavan Kumar, A. R. Supka, P. Lemoine, O. I. Lebedev, B. Raveau, K. Suekuni, V. Nassif, R. Al Rahal Al Orabi, M. Fornari and E. Guilmeau, *Adv. Energy Mater.*, 2019, **9**, 1803249.

21 V. Pavan Kumar, L. Paradis-Fortin, P. Lemoine, V. Caignaert, B. Raveau, B. Malaman, G. Le Caër, S. Cordier and E. Guilmeau, *Inorg. Chem.*, 2017, **56**, 13376–13381.

22 V. Pavan Kumar, T. Barbier, V. Caignaert, B. Raveau, R. Daou, B. Malaman, G. Le Caër, P. Lemoine and E. Guilmeau, *J. Phys. Chem. C*, 2017, **121**, 16454–16461.

23 P. Qiu, T. Zhang, Y. Qiu, X. Shi and L. Chen, *Energy Environ. Sci.*, 2014, **7**, 4000.

24 G. Guélou, A. V. Powell and P. Vaqueiro, *J. Mater. Chem. C*, 2015, **3**, 10624–10629.

25 V. Pavan Kumar, T. Barbier, P. Lemoine, B. Raveau, V. Nassif and E. Guilmeau, *Dalt. Trans.*, 2017, **46**, 2174.

26 S. O. J. Long, A. V Powell, P. Vaqueiro and S. Hull, *Chem. Mater.*, 2018, **30**, 456–464.

27 H. Xie, X. Su, G. Zheng, T. Zhu, K. Yin, Y. Yan, C. Uher, M. G. Kanatzidis and X. Tang, *Adv. Energy Mater.*, 2017, **7**, 1601299.

28 T. Barbier, D. Berthebaud, R. Frésard, O. I. Lebedev, E. Guilmeau, V. Eyert and A. Maignan, *Inorg. Chem. Front.*, 2017, **4**, 424.

29 Y. Shen, C. Li, R. Huang, R. Tian, Y. Ye, L. Pan, K. Koumoto, R. Zhang, C. Wan and Y. Wang, *Sci. Rep.*, 2016, **6**, 32501.

30 M. L. Liu, F. Q. Huang, L. D. Chen and I. W. Chen, *Appl. Phys. Lett.*, 2009, **94**, 202103.

31 H. Yang, L. A. Jauregui, G. Zhang, Y. P. Chen and Y. Wu, *Nano Lett.*, 2012, **12**, 540–545.

32 C. Bourgès, P. Lemoine, O. I. Lebedev, R. Daou, V. Hardy, B. Malaman and E. Guilmeau, *Acta Mater.*, 2015, **97**, 180–190.

33 P. Lemoine, V. Pavan Kumar, G. Guélou, V. Nassif, B. Raveau and E. Guilmeau, *Chem. Mater.*, 2020, **32**, 830.

34 C. Bourgès, Y. Bouyrie, A. R. Supka, R. Al Rahal Al Orabi, P. Lemoine, O. I. Lebedev, M. Ohta, K. Suekuni, V. Nassif, V. Hardy, R. Daou, Y. Miyazaki, M. Fornari and E. Guilmeau, *J. Am. Chem. Soc.*, 2018, **140**, 2186–2195.

35 C. Candolfi, G. Guélou, C. Bourgès, A. R. Supka, R. Al Rahal Al Orabi, M. Fornari, B. Malaman, G. Le Caër, P. Lemoine, V. Hardy, J. Zanotti, R. Chetty, M. Ohta, K. Suekuni and E. Guilmeau, *Phys. Rev. Mater.*, 2020, **4**, 025404.

36 G. Guélou, C. Couder, A. Bourhim, O. I. Lebedev, N. Daneu, F. Appert, J. Juraszek, P. Lemoine, L. Segreto and E. Guilmeau, *Acta Mater.*, 2020, **195**, 229–239.

37 K. Suekuni, Y. Shimizu, E. Nishibori, H. Kasai, H. Saito, D. Yoshimoto, K. Hashikuni, Y. Bouyrie, R. Chetty, M. Ohta, E. Guilmeau, T. Takabatake, K. Watanabe and M. Ohtaki, *J. Mater. Chem. A*, 2019, **7**, 228–235.

38 P. Baláž, *J. Mater. Sci.*, 2004, **39**, 5097–5102.

39 M. Baláž, E. Dutková, Z. Bujňáková, E. Tóthová, N. G. Kostova, Y. Karakirova, J. Briančin and M. Kaňuchová, *J. Alloys Compd.*, 2018, **746**, 576–582.

40 T. Barbier, S. Rollin-Martinet, P. Lemoine, F. Gascoin, A. Kaltzoglou, P. Vaqueiro, A. V. Powell and E. Guilmeau, *J. Am. Ceram. Soc.*, 2016, **99**, 51–56.

41 X. Lu and D. T. Morelli, *Phys. Chem. Chem. Phys.*, 2013, **15**, 5762–6.

42 S.-Y. Kim, S.-G. Kwak, J.-H. Pi, G.-E. Lee and I.-H. Kim, *J. Electron. Mater.*, 2019, **48**, 1857.

43 D. P. Weller and D. T. Morelli, *J. Alloys Compd.*, 2017, **710**, 794–799.

44 P. Baláž, E. Guilmeau, N. Daneu, O. Dobrozhan, M. Baláž, M. Hegedus, T. Barbier, M. Achimovičová, M. Kaňuchová and J. Briančin, *J. Eur. Ceram. Soc.*, 2020, **40**, 1922–1930.

45 V. Pavan Kumar, G. Guélou, P. Lemoine, B. Raveau, A. R. Supka, R. Al Rahal Al Orabi, M. Fornari, K. Suekuni and E. Guilmeau, *Angew. Chemie - Int. Ed.*, 2019, **58**, 15455–15463.

46 G. Guélou, V. P. Kumar, A. Bourhim, P. Lemoine, B. Raveau, A. Supka, O. I. Lebedev, R. Al Rahal Al Orabi, M. Fornari, K. Suekuni and E. Guilmeau, *ACS Appl. Energy Mater.*, 2020, **3**, 4180–4185.

47 L. Paradis-Fortin, G. Guélou, V. Pavan Kumar, P. Lemoine, C. Prestipino, O. Merdrignac-Conanec, G. R. Durand, S. Cordier, O. I. Lebedev and E. Guilmeau, *J. Alloys Compd.*, 2020, **831**, 154767.

48 V. Pavan Kumar, L. Paradis-Fortin, P. Lemoine, G. Le Caër, B. Malaman, P. Boullay, B. Raveau, G. Guélou and E. Guilmeau, *ACS Appl. Energy Mater.*, 2019, **2**, 7679–7689.

49 M. Baláž, N. Daneu, M. Rajňák, J. Kurimský, M. Hegedüs, E. Dutková, M. Fabián, M. Kaňuchová and P. Baláž, *J. Mater. Sci.*, 2018, **53**, 13631.

50 M. Hegedüs, M. Baláž, M. Tešinský, M. Sayagues, P. Siffalovic, M. Kruľaková, M. Kaňuchová, J. Briančin, M. Fabián and P. Baláž, *J. Alloys Compd.*, 2018, **768**, 1006.

51 P. Baláž, M. Hegedüs, M. Achimovičová, M. Baláž, M. Tešínsky, E. Dutková, M. Kaňuchová and J. Briančin, *ACS Sustain. Chem. Eng.*, 2018, **6**, 2132.

52 M. Hegedüs, P. Baláž, M. Baláž, P. Siffalovic, N. Daneu, M. Kaňuchová, J. Briančin and M. Fabián, *J. Mater. Sci.*, 2018, **53**, 13617–13630.

53 P. Baláž, M. Hegedüs, M. Baláž, N. Daneu, P. Siffalovic, Z. Bujňáková, E. Tóthová, M. Tešínsky, M. Achimovičová, J. Briančin, E. Dutková, M. Kaňuchová, M. Fabián, S. Kitazono and O. Dobrozhan, *Prog. Photovoltaics Res. Appl.*, 2019, **27**, 798.

54 C. L. Azanza Ricardo, M. S. Su'ait, M. Müller and P. Scardi, *J. Power Sources*, 2013, **230**, 70–75.

55 E. Isotta, C. Fanciulli, N. M. Pugno and P. Scardi, *nanomaterials*, 2019, **9**, 762.

56 E. Isotta, N. M. Pugno and P. Scardi, *Powder Diffr.*, 2019, **34**, S42–S47.

57 P. Baláž, M. Hegedüs, M. Reece, R. Zhang, I. Škorvánek, J. Briančin, M. Baláž, M. Tešinský and M. Achimovičová, *J. Electron. Mater.*, 2019, **48**, 1846.

58 Y. Bouyrie, M. Ohta, K. Suekuni, P. Jood and T. Takabatake, *J. Alloys Compd.*, 2018, **735**, 1838–1845.

59 J. Rodríguez-Carvajal, *Phys. B*, 1993, **192**, 55–69.

60 T. Roisnel and J. Rodríguez-Carvajal, *Mater. Sci. Forum*, 2001, **378**–**381**, 118–123.

61 H. S. Kim, Z. M. Gibbs, Y. Tang, H. Wang and G. J. Snyder, *APL Mater.*, 2015, **3**, 041506.

62 E. Alleno, D. Bérardan, C. Byl, C. Candolfi, R. Daou, R. Decourt, E. Guilmeau, S. Hébert, J. Hejtmanek, B. Lenoir, P. Masschelein, V. Ohorodnichuk, M. Pollet, S. Populoh, D. Ravot, O. Rouleau and M. Soulier, *Rev. Sci. Instrum.*, 2015, **86**, 011301.

63 J. R. Craig and P. B. Barton, *Econ. Geol.*, 1973, **68**, 493.

64 P. E. Lippens, *Phys. Rev. B*, 1999, **60**, 4576–4586.

65 P. G. Spry, S. Merlino, Su Wang, Xiaomao Zhang and P. R. Buseck, *Am. Mineral.*, 1994, **79**, 750–762.